PAPER

Screening current rotation effects: SCIF and strain in REBCO magnets

IOP Publishing Superconductor Science and Technology
Supercond. Sci. Technol. **34** (2021) 095004 (12pp) https://doi.org/10.1088/1361-6668/ac1525

Screening current rotation effects: SCIF and strain in REBCO magnets

D Kolb-Bond[1,*], M Bird[1], I R Dixon[1], T Painter[1], J Lu[1], K L Kim[1], K M Kim[1], R Walsh[1] and F Grilli[2]

[1] NHMFL, Florida State University, Tallahassee, FL, United States of America
[2] Institute for Technical Physics, Karlsruhe Institute of Technology, 76131 Karlsruhe, Germany

E-mail: kolb-bond@magnet.fsu.edu

Received 15 February 2021, revised 17 June 2021
Accepted for publication 16 July 2021
Published 5 August 2021

Abstract

Screening currents and their effect on the magnetic field and strain state have been shown to be a major problem in the design and operation of rare-earth-barium-copper-oxide magnets, distorting the field and rotating the conductor to potentially large strains. The latter is a possible catalyst for damage as both plastic deformation and degradation of the critical current leading to reduced fatigue life or even catostrophic failure. Due to the nonlinear dynamic behavior of the screening currents and the significant possible rotation, including this rotational effect in the electromagnetic state requires a new addition to the existing models. The effect of the changing rotation angle of the conductor on the electromagnetic and stress state is investigated by using a modified homogeneous *T*–*A* method. Numerical results are compared with experimental tests.

Keywords: coupled mechanical and electromagnetic analysis, 2G HTS magnet, large-scale superconductor systems, screening currents

(Some figures may appear in colour only in the online journal)

1. Introduction

Whether the topic has been the screening current induced field (SCIF) or the plastic deformation from the torque generated, screening current calculations have been an important subject for many years by several groups working on the design of ultra-high field magnets using rare-earth-barium-copper-oxide (REBCO) tape [1–12]. Early work in the field showed decent agreement between computed and measured SCIF [3–5, 8, 11]. Traditional calculations for solenoids assume the REBCO tapes are parallel to the axis after winding and compute screening current distributions via several different electromagnetic models. More recently, these computed screening currents were crossed with the magnetic field distribution to calculate the diamagnetic torques on the tapes and the resulting twist and strain [13–15]. In 2019 results were presented by a few different groups indicating that these calculations did not agree well with measured strain values [16–18].

It has been previously noted that the rotation itself is affecting the electromagnetic distribution by changing the normal field component [15, 16]. Herein we present an updated approach to the computation of screening currents by including an iterative coupling of the electromagnetic calculation of screening current with the displacement calculation of the rotation of the tapes.

2. Calculations: electromagnetic

The heart of the improvement is the dynamically changing rotation angle of the conductor and the coupling of this rotation to the electromagnetic equations (figure 1). The changing local rotation angle of the conductor (α) directly impacts (a) the normal field component to the tape (B_n) and (b) the local critical current density of the high temperature superconductor (HTS) (J_c). These modified equations are:

$$B_n = B_r \cos(\alpha) - B_z \sin(\alpha) \quad (1)$$

* Author to whom any correspondence should be addressed.

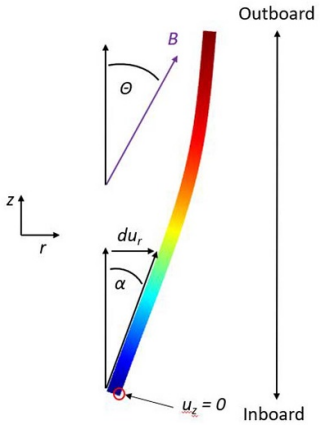

Figure 1. Definition of the local conductor rotation angle, α and magnetic field angle, Θ, shown on a conductor cross section. Colors note the strain distribution as an example. Negative strain in blue to positive in red.

$$B_{\mathrm{p}} = B_z \cos(\alpha) - B_{\mathrm{r}} \sin(\alpha) \tag{2}$$

$$\frac{\mathrm{d}B_{\mathrm{n}}}{\mathrm{d}t} = \left(\frac{\mathrm{d}B_{\mathrm{r}}}{\mathrm{d}t}\cos(\alpha) - \frac{\mathrm{d}B_z}{\mathrm{d}t}\sin(\alpha)\right) - \frac{\mathrm{d}\alpha}{\mathrm{d}t}\left(B_{\mathrm{r}}\sin(\alpha) + B_z\cos(\alpha)\right) \tag{3}$$

$$J_{\mathrm{c}} = J_{\mathrm{c0}} \Big/ \left(1 + \frac{\sqrt{k^2 {B_{\mathrm{p}}}^2 + {B_{\mathrm{n}}}^2}}{B_0}\right)^{-\mu} \tag{4}$$

$$\alpha = \tan^{-1}\left(\frac{\mathrm{d}u_{\mathrm{r}}}{\mathrm{d}z}\right). \tag{5}$$

Equations (1) and (2) are the normal and parallel magnetic field components relative to the conductor axis. This varies along the width of a turn of conductor due to elastic deformation. Only the time derivative of the normal field component (equation (1)) is taken for equation (3) because we consider only the normal field induction as dominant (elaborated on in section 10). The J_{c} fit (equation (4)) was taken from [12, 19] and modified to add the relative field to the conductor with equations (1) and (2). Equation (5) is the local rotation angle as a function of the conductor displacement.

The first term of equation (3) (the ramp term) indicates that as the conductor rotates, the normal field component decreases until the conductor is parallel with the field angle ($\alpha = \Theta$) at which point the normal field component (B_{n}), which induces the screening current, is zero. At this point no new screening currents are generated, and the super-currents already generated will persist. If α were greater than Θ, B_{n} will be negative, and negative screening currents and negative torque will be generated, rotating the conductor backwards to the field angle. The conductor is thus effectively rotation-limited by the field angle and should settle to a stable equilibrium neglecting outside forces. Because of the small field angle near the midplane of a solenoid, the consequence of this field angle equilibrium is computed strains near the mid-plane of a solenoid that are significantly less than in the traditional model (shown in section 9). The second term of equation (3) (the rotation term) is coupled to the 'ramp term' in a high field coil. This term generates screening currents to oppose the manual rotation (represented by the negative sign in front of $\mathrm{d}\alpha/\mathrm{d}t$). A conductor placed into a uniform background field and manually rotated (conductor or field rotation) will generate screening currents (and torque) even if the background field is not changing with time.

The effect of equation (4) can be contrary to that of equation (3). As the conductor rotates towards being parallel with the field angle, the critical current density increases dramatically. For some coils, the traditional uncoupled approach indicates that the turns of end pancakes are operating at saturated current density on their two halves [10, 14, 19]. Equation (4) indicates end turns (where the field angle is large and large rotation angles are possible) might carry significantly more screening current than the traditional models indicate, rotating out of the saturated state. It is the balance between these two effects that creates the new results shown herein.

3. Calculations: structural

Including the rotation requires a coupling between the electromagnetic and the structural models. The equations (3) and (4) ask for the rotation angle (α) at every time step, requiring the displacements from the structural model to be solved in parallel. To do this efficiently, one utilizes a similar 'submodel' of the structural model as shown previously in [15] where the electromagnetic forces are mapped onto the structural model to compute the displacement field. Our new addition is mapping of the rotation angle back onto the electromagnetic model by calculating the local rotation angle (equation (5)) as a function of the radial displacement, u_{r} and the magnet axis, z. The time derivative of equation (5) is numerically calculated at each timestep.

Our new model, geographically christened 'FLOSSS' (Florida Screening Strain Software) consists of two separate models, the electromagnetic and structural, coupled together at each timestep. We use $V1$ to refer to the original model without rotation coupling (i.e. $\alpha = 0$) [15] and $V2$ to refer to the new model that includes the rotation coupling through equations (3) and (4) and illustrated in figure 2. This figure shows how a single pancake is coupled using the two models. The coupling or 'mapping' between the models should be broached carefully to maintain accuracy. The models consisting of different geometric distributions carry an intrinsic approximation as there is not a 1:1 application of the Lorentz forces or rotation angles. When including the non-current carrying co-wound reinforcement in the structural model it is mapped onto the conductor by the ratio of the area of the separate turns. The rotation angle is mapped onto the entire pancake in the electromagnetic model. For implementation both maps are done in COMSOL Multiphysics using the general extrusion operator. The maps are made onto the initial geometric entities

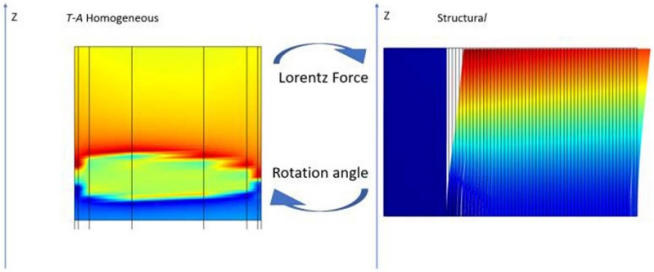

Figure 2. Illustration of a single pancake of an example coil with the two axisymmetric models coupled in FLOSSS *V*2. Left: *T–A* homogenous model showing screening current distribution Right: structural submodel showing strain field and displacement. In both left and right the color scale is negative in blue to positive of red.

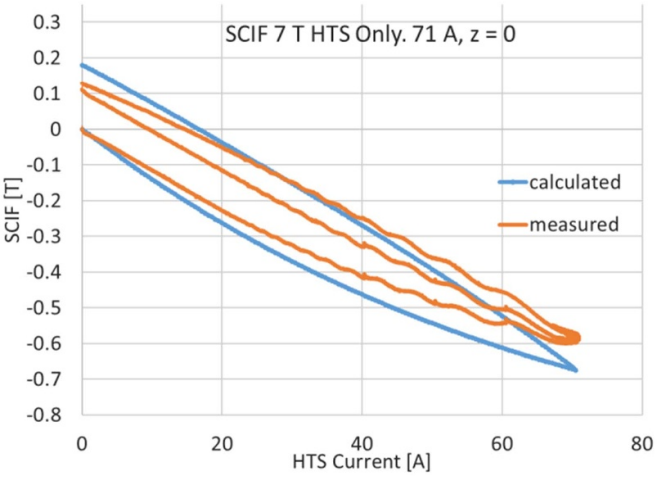

Figure 3. SCIF plot showing agreement at low field and current.

with 0 displacement (shown in wireframe on the right model of figure 2) and not the displaced ones.

Submodeling the structural model has numerous benefits besides the more physical geometry and properties. It allows us to use the efficiency of the *T–A* homogeneous model while including all the structural features present in the physical coil as in the *T–A* homogeneous model we do not need to model every turn of winding while the structural model requires modeling of every turn of winding for accurate displacement calculations. Another benefit is that all the pancakes do not need to be submodelled. If the peak torque location is known, by using an approximate model, field alignment or other heuristics, then the number of pancakes to submodel can be limited to a select few.

4. Results: SCIF

The SCIF as noted earlier is defined as the field B_e (including screening current distributions in the HTS) minus the nominal field B_0 (assuming uniform current density from only the transport current). The SCIF is then plotted as a function of the nominal field or $B_{\mathrm{SCIF}}(B_0) = B_e - B_0$. It is an effective way to look at the overall contribution of screening currents on the magnetic field. The results shown assume central SCIF (r and

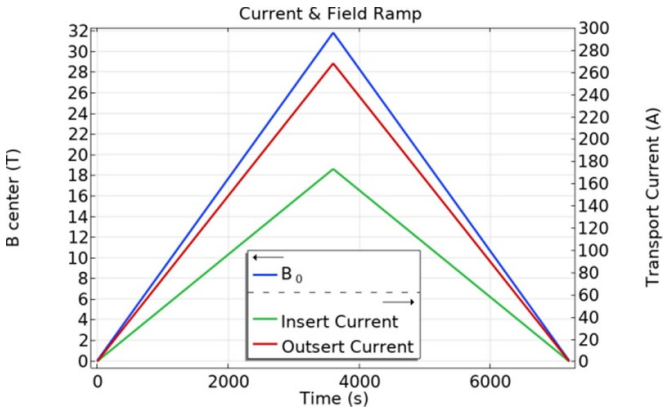

Figure 4. 32 T ramp profile. Blue: central field at $r,z = 0,0$. Green: transport current in HTS insert. Red: transport current in LTS outsert.

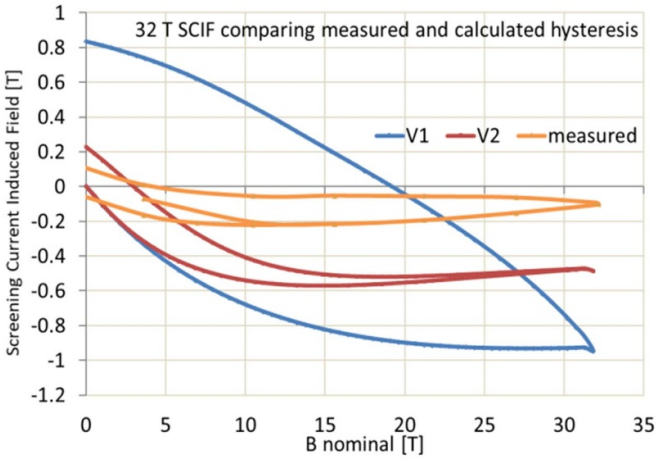

Figure 5. 32 T SCIF showing original *T–A* model (*V*1), measured SCIF and new calculation including the rotation coupling (*V*2).

$z = 0$) unless stated otherwise. The 32 T all-superconducting magnet at the NHMFL [20] has had the SCIF measured at low and high field with Hall and nuclear magnetic resonance (NMR) probes respectively. Initial measurements were taken of the field due to the inner (high temperature superconducting) coils only running to 41% of nominal current. They agreed well with calculations using FLOSSS *V*1 (which assumes 0 rotation angle) (figure 3). The calculations and measurements started at zero current in the HTS coils. In the calculation we assume zero initial SCIF and zero initial SCIF was measured in the magnet. Current was increased to ∼70 A with a linear ramp over 3600 s and the SCIF reached −0.6 T. As current was reduced, the SCIF returned to near zero. There is a positive residual SCIF. Current was then run back up to 70 A. The oscillations in the measured values as the current exceeds 20 A are believed to be artificial and due to quantum oscillations in the Hall sensor.

However, when the combined HTS and low temperature superconducting (LTS) coils were energized to full field of 32 T and then de-energized as per the ramp (figure 4) the peak measured and computed SCIF values using FLOSSS *V*1 disagreed at full current by a factor of ∼9 (figure 5). In addition,

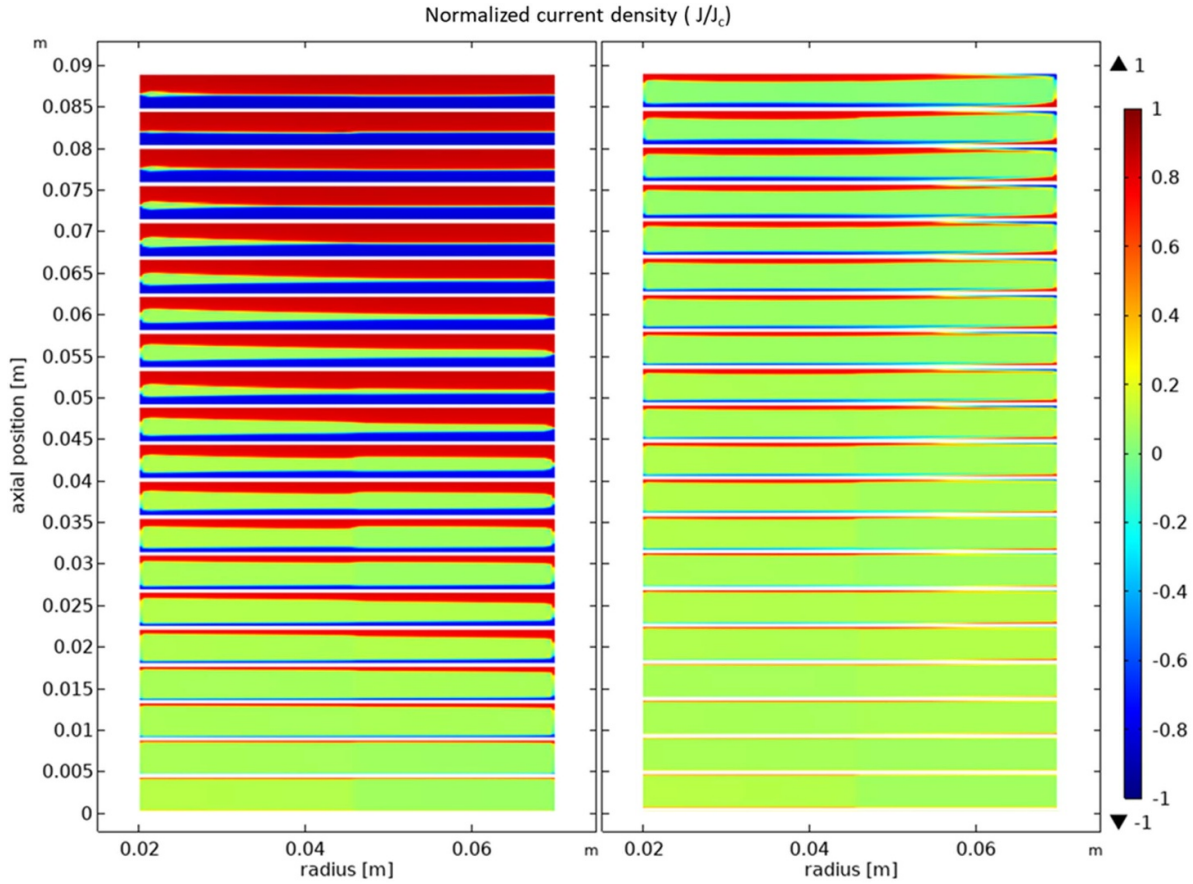

Figure 6. 32 T coil 1 upper half plotting normalized current density distributions at full field (3600 s in figure 4). Left: $V1$ plot showing large saturation. Right: $V2$ calculation. Note screening current reversal at OD where the rotation angle is momentarily greater than the field angle.

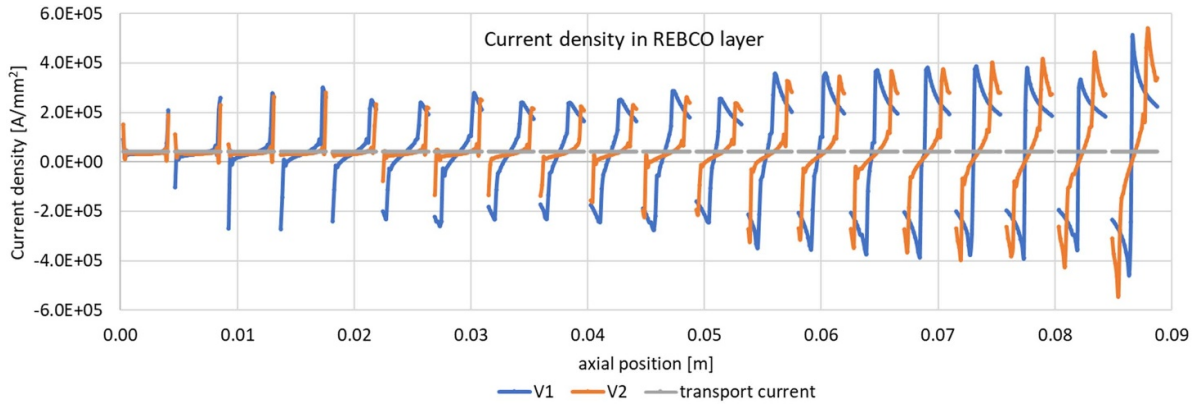

Figure 7. 32 T coil 1 current density in ID turns at full field (3600 s). Comparing $V1$, $V2$ and transport current only. Near the midplane the $V2$ calculation shows minimal screening currents due the small field angle. At the ends the $V1$ and $V2$ calculations are more similar but $V2$ currents flow nearer the edges due to the higher critical current.

the shape of the computed and measured curves of SCIF vs current were quite different with the ramp from full current to zero being computed to be concave down and measured to be concave up. In this case the field was measured with an NMR probe and the first measurement was at 4 T with −0.05 T SCIF. The magnet was taken to 32 T and then ramped down to −32 T and back up to +32 T. Only the region with positive field is shown. We see that for field >12 T the SCIF seems to be independent of the starting SCIF.

Figure 5 also shows the computed SCIF using FLOSSS $V2$ (coupled rotation and electromagnetic calculations with sub-modeling). The computed SCIF magnitude at full current is better by a factor of 2 but still off from the measured value by a factor of 5. The overall shape is closer as well with the SCIF during ramp down being concave up in both the measured and computed results. The SCIF is a direct response to the different current density distributions shown in figures 6 and 7. In figure 6 the normalized current density distributions

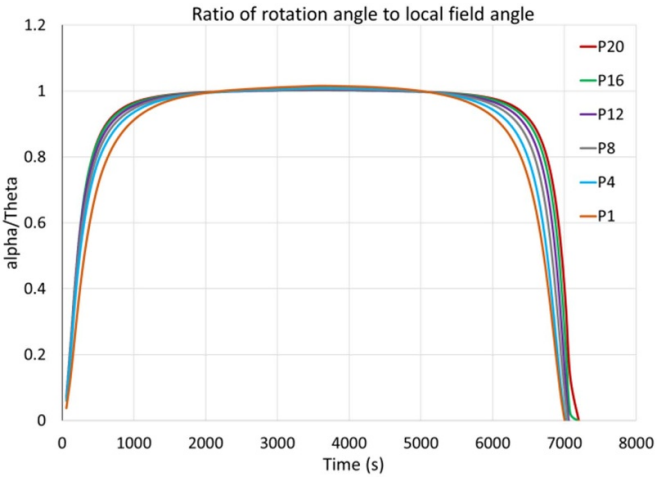

Figure 8. 32 T coil 1 α/Θ of each pancake, numbered starting at the end pancake. Θ includes the screening current distribution.

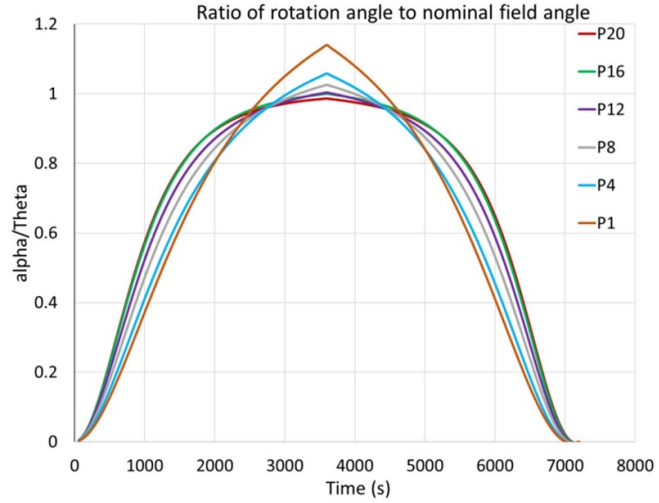

Figure 9. 32 T coil 1 α/Θ of each pancake, numbered starting at the end pancake. Θ does not include the screening current distribution.

of $V1$ and $V2$ are plotted. In particular the saturation of $V1$ is noticeable in contrast with $V2$ where the conductor can rotate into a higher critical current and out of the saturation. In figure 7 we plot the current density in the 1 μm REBCO layer for $V1$, $V2$ and transport current (neglecting any screening current distribution) for the first turn at the inner diameter (ID).

The ratio of rotation angle to field angle (both taken at the outer diameter (OD) at the center width of each pancake) is plotted (figures 8 and 9). The field angle in figure 8 includes the field generated by local screening currents while the field angle in figure 9 only considers a uniform current density from the power supply. Note that the rotation angle in figure 8 has an equilibrium at the field angle. Local rotation angles exceeding the local field angle return to equilibrium at the field angle by negative torque (from negative B_n in equation (3) Because the coil system is ramped simultaneously the field angle is effectively constant and defined by the geometry (neglecting the

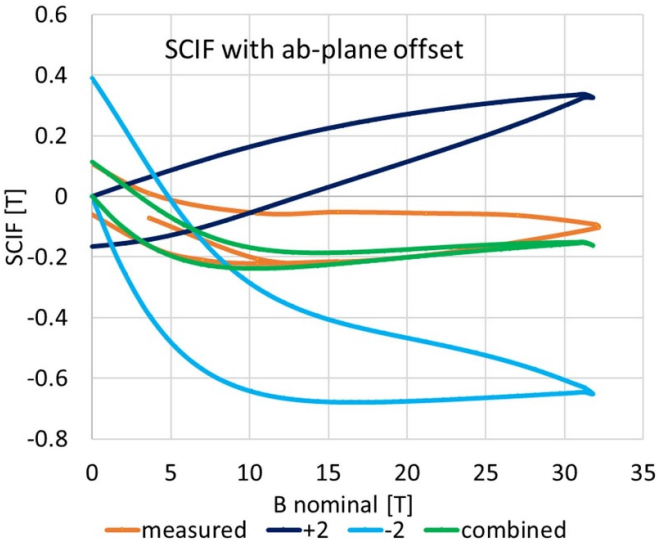

Figure 10. 32 T SCIF showing measured, $+2^\circ$, -2° and the asymmetric combination.

screening currents affect on the field angle) figure 9 shows the same ratio of rotation angle to field angle but considering the field angle due to only uniform current density in the coil system (0 screening currents contribution). Note how most of the coil is limited by the field angle with the exception of the end pancakes (P1-4). It is suggested the screening current contribution from the rest of the pancakes on these individual pancakes adds to the local radial field and thus significantly increases the field angle and the end while the inner midplane pancakes are less affected. Note how in figure 8 with the contribution of screening currents on the field distribution that the rotation aligns with the field for all pancakes at $\sim$2000 s or $\sim$18 T. This only shows the local rotation angle at one point on each pancake and does not reflect the distribution over the rest of the pancake (discussed in section 6).

5. Results: SCIF and *ab*-plane offset

It should be noted that the field-angle, Θ, is <5° over 50% of the magnet. With such a small field-angle and the rotation angle equilibrium at the field angle, the *ab*-plane offset [21–23] of (0°–3°) should be an important effect as it changes the effective field angle on the conductor by $\pm$ the *ab*-plane offset depending on the conductor orientation. It is unfortunate that the *ab*-plane offset orientation was not tracked during winding of the 32 T magnet to know the orientation of each conductor of each pancake of the coil stack, however, we perform calculations for three cases: (a) all tapes have the *ab*-plane at $+2^\circ$, (b) all tapes have the *ab*-plane at -2°, and (c) The bottom half of the coil being at -2° and the top half at $+2^\circ$. In figure 5 above we assumed zero *ab*-plane offset.

This offset was applied as an initial rotation angle constant α_0 ($\alpha_e = \alpha + \alpha_0$) that affects both the critical current and inductive normal field. The energization cycle uses the same profile as figure 4. Results are presented in figure 10.

Table 1. Stress analysis model key parameters: MFC.

Material parameters	Thickness, width (mm)	(E_r, E_z, E_θ) (GPa)
REBCO tape	0.095, 4	100, 143, 143
Cowind	0.50, 4	15, 15, 15
Mandrel	1.5, 4	15, 15, 15
Coil parameters	**Values**	**Units**
Inner radius, outer radius	60, 60.725	mm
Turns	5	
Operating current	400	A
Background field	12	T

With the -2° curve, we see the largest magnitude at peak field as well as the greatest difference between the curves for increasing and decreasing current. The $+2^\circ$ curve magnitude is positive (wrong sign) but, more remarkably, the hysteresis loop travels in the opposite direction. We see that the measured SCIF curve falls between the computed -2° and $+2^\circ$ curves which (a) indicates that including the rotation of the tape has reduced the discrepancy between measured and computed SCIF to less than the uncertainty associated with the assembly process and (b) suggests that if we knew how the pancakes were wound and assembled, the agreement between measured and computed values might be much better. However, neither a $+2^\circ$ or -2° offset angle is likely in the real magnet. This would mean that all the pancakes in the bottom end of the magnet would be stacked with the offset angle 'down' while those in the top are stacked with the offset 'up'. This seems very unlikely to have happened by accident. We would expect either the orientation of the various (112) pancakes would be random, or most of them in a coil would be the same direction which would mean the offset angles in the top and bottom halves of the coils are of opposite sign. Consequently, we re-computed the SCIF assuming $+2^\circ$ for the top half of both coils and -2° for the bottom half. We see that this assumption (combined) leads to the best agreement yet with the measured value. When the current increases from 15 T to 25 T, the ratio of computed to measured values using $V2$ are typically 1.05, much better than the ratio of $\sim$9 that we saw with $V1$ at peak field. Between 25 T and 32 T, there is some discrepancy between the measurements and calculations which gets much larger during the entire de-energization to 0 T.

6. Results: strain

In 2020 the 'Mini Fatigue Coil' (MFC) consisting of five turns in a single pancake was built including two strain gauges (table 1 and shown in figure 11) and tested to determine how well the new algorithm works for computing strains. With no adjacent pancakes there is no axial compression, friction on the pancake edges, or local screening currents from adjacent pancakes which all simplify the problem.

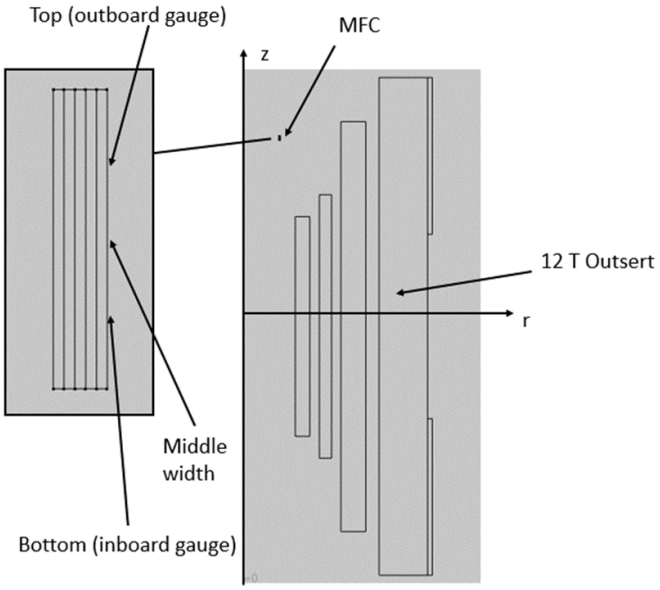

Figure 11. The geometry of the MFC and 12 T LTS system. Gauges are placed 1 mm from middle width of conductor.

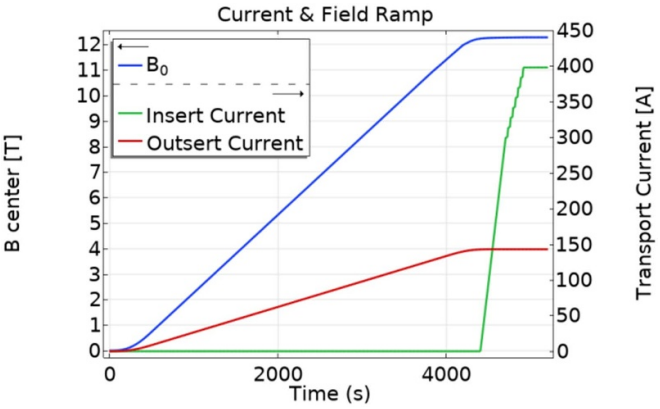

Figure 12. Energization profile of the MFC system. Blue: center field of combined system. Red: the outsert is ramped to full-field and held. Blue: the insert (green) is ramped linearly and then step ramped to imitate physical experiment.

There is also neither co-wound reinforcement nor external over-banding reinforcement, only the Kapton insulation which is co-wound with the conductor onto a G10 mandrel. The coil was installed 255 mm above the mid-plane of a 14 T large bore magnet that provided background field (to 12 T). By being offset from the mid-plane the nominal magnetic field makes an angle of $\sim 7^\circ$ to the tape surface and there is resulting diamagnetic torque and twist.

The REBCO tape is 4 mm wide. The strain gauges were 0.5 mm wide and were placed with their centers 1.0 mm from the centerline of the REBCO tape. Thus, each gauge records the average strain over a 5.8 mm gauge length in the region 0.75–1.25 mm above or below the centerline of the REBCO tape.

The test energization shown in figure 10 consisted of ramping the outsert magnet from 0 T to 12 T with zero transport

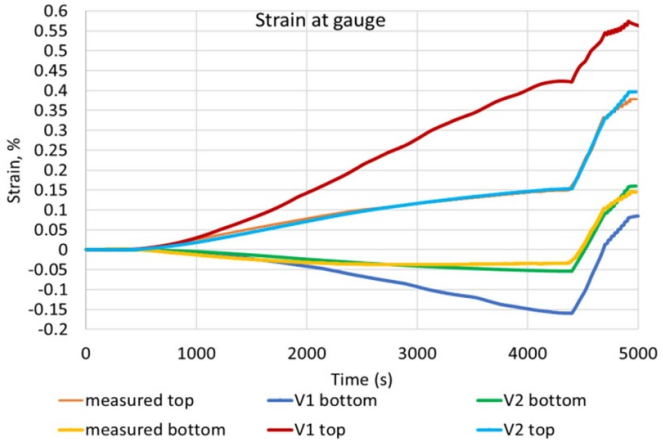

Figure 13. MFC calculation showing the calculated $V1$, $V2$ and measured strain on the gauges.

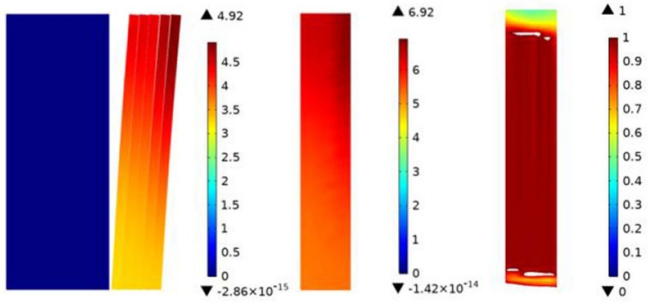

Figure 14. MFC calculation showing the calculated rotation angle. Left: angle calculated on displaced geometries. Middle: mapped rotation angle including *ab*-plane offset. Right: α/Θ scaled between 0 and 1. White areas are >1 assumed to be local bending and will generate negative torque. Note ratio is small at outboard edge where radial field from the insert is larger.

current in the HTS insert coil. During this period (0–4300 s in figure 12) screening currents are generated in the REBCO tape which puts the edge closer to the mid-plane of the magnet in compression and the edge further from the mid-plane into tension. Then the insert HTS coil was energized from 0 to 400 A (4300–4900 s in figure 12). During this period the transport current interacts with the background field to produce mostly net tension at both gauges.

A roller corner condition is applied to the inboard edge of the outer diameter of each turn. (The axial displacement, u_z, of each turn of conductor is constrained to be zero on the corner of the cross-section towards the mid-plane of the background magnet and at the outer diameter of the turn.). The calculation strain is taken as a point strain 1 mm from the center width (the location of the strain gauges). We apply our $+2^\circ$ offset with and without the rotation coupling in our comparison. Since our model is now fully dynamic, we can compare not only magnitudes but the shape of both curves.

The results using $V2$ show good agreement overall and especially after ramping the outsert (figure 13). The outboard gauge after ramping the outsert agrees well at 0.15%. At full field both gauges have agreement to within <0.02% strain. It

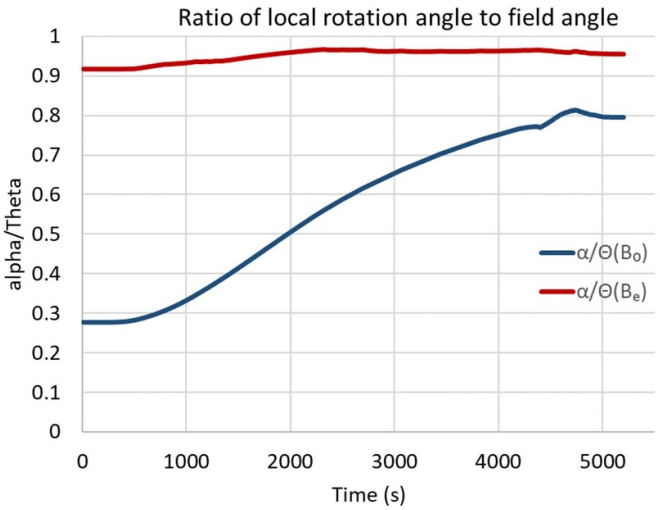

Figure 15. Ratio of rotation angle to field angle with and without screening currents. Note while the rotation follows the local field angle the total rotation to the nominal field angle occurs mostly from the background field ramp and does not exceed the nominal field angle.

Table 2. Stress analysis model key parameters: PTC.

Material parameters	Thickness, width (mm)	(E_r, E_z, E_θ) (GPa)
REBCO tape	0.095, 4	100, 143, 143
Cowind	0.35, 4	200 200, 200
Mandrel	1.5, 4	15, 15, 15
Coil parameters	**Values**	**Units**
Inner radius, outer radius	50, 54	mm
Number of disks	12	
Turns per disk	41	
Operating current	370	A
Background field	6.5	T

is noted that there is a negative strain, compressive from the screening current rotation. We are measuring and calculating strain due only to screening currents as the conductor does not have transport current prior to 4300 s. The inclusion of both the rotation coupling and *ab*-plane offset angle are responsible for the good agreement shown here.

Figure 14 plots the distribution of rotation angle for the structural model, electromagnetic model, and the ratio of rotation angle to local field angle.

Figure 15 shows the rotation angle ratio to field angle at the OD of the pancake and center width of the conductor. Note how the local rotation angle follows the local field angle (including screening currents) but starts lower from the field angle (neglecting screening currents) the rotation angle is limited here again by the local field angle. Note also how most of the rotation happens due to the background field but does not reach $\geqslant 1$ (as in the 32 T case).

This coil was later cycled ~24 000 times at a measured strain of 0.38% at the outboard gauge and 0.15% strain at the

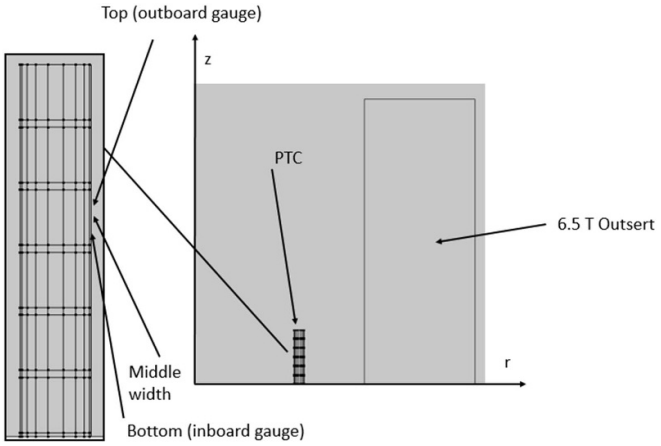

Figure 16. The geometry of the PTC and 6.5 T LTS system. Gauges are placed 1 mm from middle width of conductor.

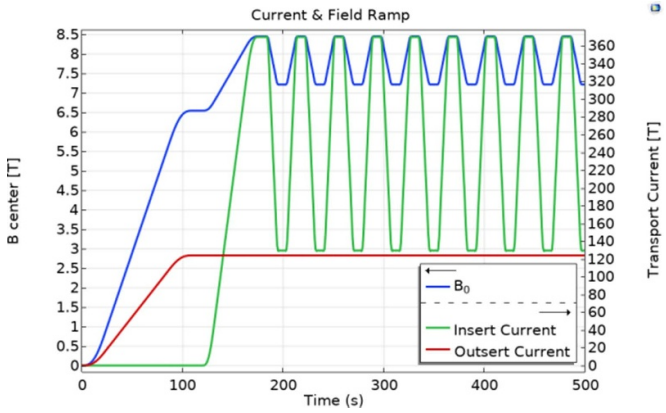

Figure 17. PTC cycling. Outsert is ramped and then insert is cycled with a trapezoid ramp shape. Linearly ramped up/down and held.

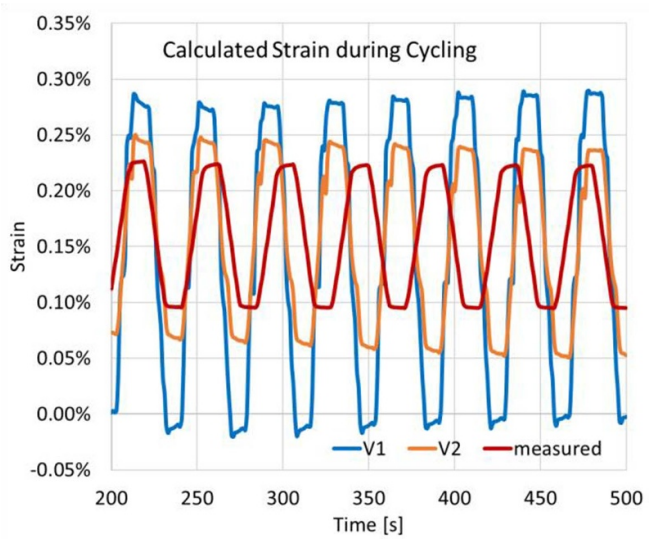

Figure 18. PTC cycling showing differences between the $V1$, $V2$, and measured strain.

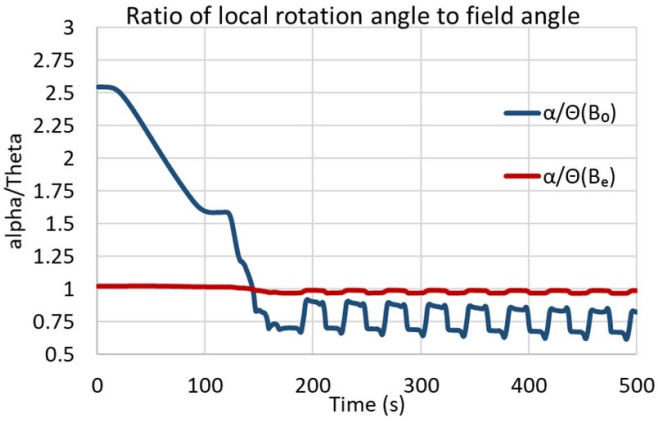

Figure 19. PTC with ratios of the local rotation angle to the local field angle with and without screening current contributions.

inboard gauge. A linear fit of the two measured strains gives 0.49% strain at the outboard edge. As the gauges are 2 mm apart, we take the difference as continuous and linear to the edge. The computed value at this point was 54%.

Another test coil analyzed was the 'Petten Test Coil' (PTC) (table 2 and shown in figure 16) This coil was larger than the MFC but still much smaller than a real coil. It has 12 pancakes with an ID of 50 mm and OD of 54 mm. It is centered at the mid-plane in a nominal 6.5 T outsert coil. The coil was cycled 4800 times according to the energization profile of figure 17 and showed no degradation.

We compared our old model ($V1$) and our new model ($V2$ including the 2° offset) with the measured data. (figure 18) We see that the $V2$ calculations more closely approximate the cycling behavior of the measured plot. Note that the ramp rate of calculated and measured values is ∼20 A s^{-1} and ∼18 A s^{-1} respectively, resulting in a different frequency. The magnitude at maximum insert current is within 0.02% strain and is off 0.03% at minimum current.

Figure 19 shows the ratio of local rotation angle to field angle. Note how the ratio starts above the field angle because the *ab*-plane offset (2°) is greater than the field angle of the outsert field on the insert coil and the conductor starts rotating in the negative direction towards the effective field angle on the conductor. When the insert ramps the radial field contribution and thus the field angle increases and the ratio is <1.

7. Strain dependence of critical current

The critical current is known to be dependent on strain [24, 25]. At approximately 0.55% strain the conductor shows considerable critical current degradation. Above 0.7% strain, plastic deformation of the substrate can occur. The critical current shows a 12% drop from 0% to 0.55% strain and close to 100% drop at 0.9% strain (figure 20). Our calculations in the past ignored this drop-off in I_c despite giving results with strain beyond 0.55%. With our dynamic model we can calculate the effect of critical current degradation as the coil ramps. The measured data in figure 18 was taken at 77 K and our I_c fit assumes 4 K data. We assume that the degradation is the same at 4 K for the calculation.

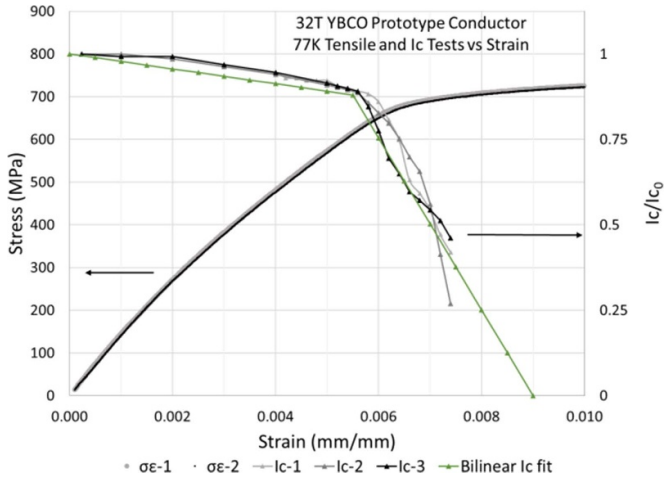

Figure 20. Both I_c and stress as a function of strain. Note the point around 0.6% where I_c drops and the conductor starts to plastically deform.

Based on figure 20 we introduce a bilinear model of $I_c(\varepsilon)$:

$$I_c(\varepsilon) = \beta(\varepsilon) I_c(B) \tag{6}$$

$$\beta = 1 - 0.12\frac{\varepsilon}{0.55\%} \quad \text{if } \varepsilon < 0.55\%$$

$$\beta = 0.88 - 0.88\frac{\varepsilon - 0.55\%}{0.9\% - 0.55\%} \quad \text{if } 0.55\% < \varepsilon < 0.9\%.$$

The modeled $\beta(\varepsilon)$ is symmetric for tensile and compressive strain. Our model uses a single turn of conductor that we assume rotates proportional to the torque ($\alpha = \gamma\tau$) with a uniform angle across the width and the axis of rotation being the center width (2 mm). From the uniform angle we find the rotational hoop strain as a function of axial distance (z) from the center width of the conductor using ($\varepsilon_r = z/r \times \sin(\alpha) = z/r \times \sin(\gamma\tau)$. The γ constant was chosen specifically so the conductor would rotate to 0.7% strain at the edge (note rotation strain at $z = 0$ is 0). A uniform transport strain component is added to the previous rotation strain as a quadratic function of the ratio of transport current ($\varepsilon_t = 0.003 \times (I/I_{op})^2$). I is the transport current as a function of time and I_{op} is the designed maximum current. This 'transport strain' has a maximum of 0.3% at full field. The total strain is then ($\varepsilon = \varepsilon_t + \varepsilon_t$). This approach approximates the structural calculation but is much simpler to solve, and has been shown to give similar results as the fully-coupled approach described in section 3 above. The parameters were set up to look at an extreme case that would result in damage as these high strain values have been calculated for coils where plastic deformation has been observed.

There is a difference between the results with and without strain dependence when the effect of rotation is ignored ($V1$), primarily above 0.7% strain. (figure 21). However, if we include the effect of rotation ($V2$), the inclusion of strain dependence makes little difference in the computed results as the rotation reduces the strain below 0.7% strain. The rotation

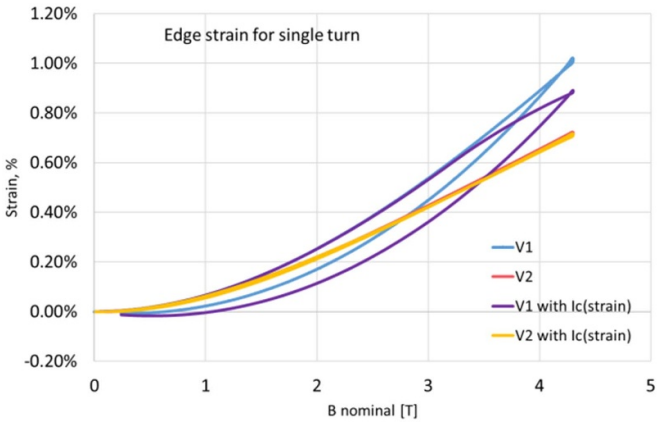

Figure 21. Strain hysteresis comparing, $V1$ and $V2$, both with and without the strain dependence of critical current ($I_c(\varepsilon)$).

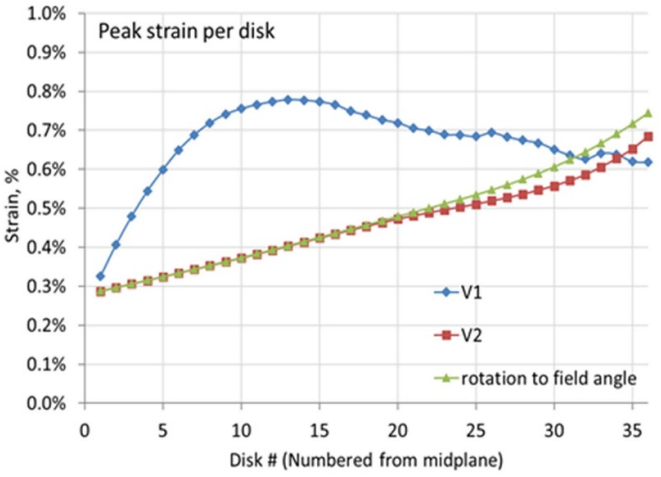

Figure 22. Comparison of field alignment with coupled rotation. $V1$ is the old model, $V2$ is the new dynamic model. Rotation to field angle is assuming the conductor rotates to the field angle and sums with the transport strain.

is more dominant than $I_c(\varepsilon)$ for the one computed cycle. The peak strain for $V2$ is ~0.65% which corresponds to 50% I_c but this is only present at the edge of the conductor due to the rotation strain, the average peak strain is still only 0.3%. We did not look at the case of starting with a degraded conductor and the irreversible damage through cycling.

8. Strain distribution including rotation

Figure 22 compares computed strain with rotation, without rotation, and the strain if the conductor rotated to the nominal field angle assuming ($\alpha = \Theta$) and the simple method from section 8. The coil is a high field coil design operating at a low fraction of critical current. Note the transport strain (ignoring screening currents) at the midplane calculated to be 0.3%. The strain points plotted are the peak values across the outboard edge at full field. It is possible that the peak strain values were larger earlier and in other locations earlier in the energization. We compute much lower strain in the 2/3 of the coil closest

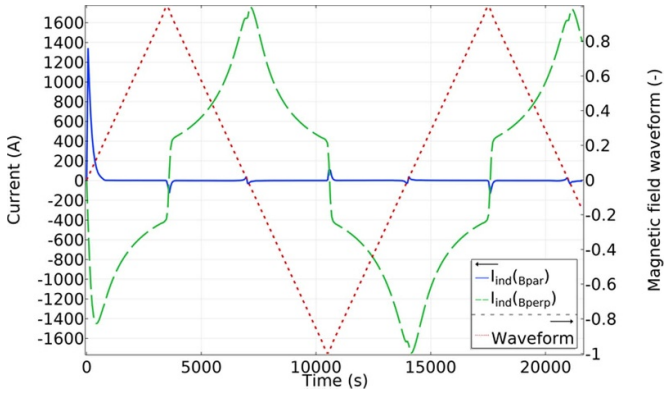

Figure 23. Evolution of the current induced in a single HTS wire by a magnetic field with amplitude components of 20 T and 4 T in the direction parallel and perpendicular to the tape's flat face. The temporal evolution of the applied field is represented by the red dashed line. Note the first ramp up contributes significant parallel field induction until around 780 s after which perpendicular field induction dominates.

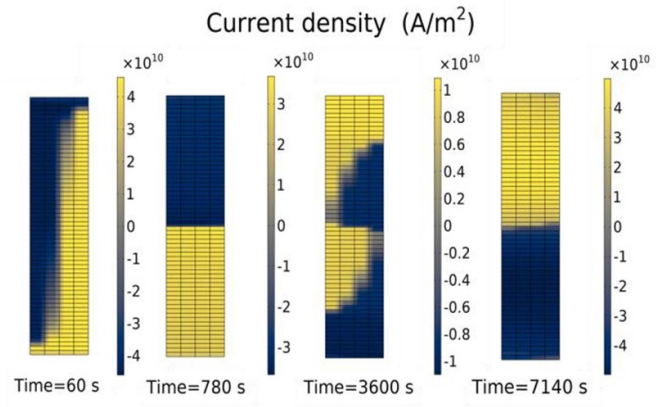

Figure 24. Current density distribution taken at $t = 60$ s, $t = 780$ s, $t = 3600$ s and $t = 7140$ s, when the amplitudes of the currents induced by the parallel field are largest, smallest, return on field reversal and when perpendicular field contribution is largest respectively (see dashed line in figure 22). Note the different current density scale. The thickness of the 4 mm tape has been artificially expanded to 10 μm to help simulation convergence. In the figure the scale in the two directions is different so that details of J can be visualized. The utilized mesh grid is also shown.

to the mid-plane (pancakes 1–24). This is because the $V1$ calculations (ignoring rotation) compute rotation beyond alignment with the field. In $V2$, when the rotation is coupled at each time-step, the normal component of field is lower and the resulting screening current, torque and twist are lower as well as becoming negative much earlier because the field angle is small. At the outmost 1/3 of the coil (disks 25–36) we see similar strain in the two calculations. In this region neither calculation gives tapes rotating to or past the field angle. However, the $V1$ calculation does not account for the increase in I_c due to the tape becoming closer to the field angle. While the $V2$ calculation has a smaller normal component of field, it has higher I_c. Hence the torque, twist, and strain are comparable. We have seen similar behavior in calculations for other coils as well.

9. Axial vs radial field magnetization

The models described herein and in most of the references consider only the currents induced by the radial field (thin film approximation) while those generated across the 1 μm thickness as a result of the axial field induction were left out of the model. While this approximation has been previously verified for ac power applications [6] it was not completely clear that it is valid in the case of high field solenoids.

We have computed the screening currents in a single tape in a background field of 20 T parallel to the tape surface (axial field) and 4 T perpendicular (radial field) (similar to the end of our 32 T magnet) with both components of inductive field included. The finite-element method simulations were performed with the H-formulation [26]. Figure 23 shows the field versus time as well as the magnitude of the computed induced currents. I_{ind} and I_{perp} are taken to be the total integral of screening currents across the width and are calculated as $\int \boldsymbol{J} \frac{x}{|x|} \mathbf{dydy}$ and $\int \boldsymbol{J} \frac{y}{|y|} \mathbf{dxdy}$ respectively. Figure 24 shows contour plots of induced currents at a few points during the cycling process. During the initial charging we see a significant influence of the axial field, but the current distribution becomes dominated by the radial field component about 780 s into a 1 h ramp. Thereafter the parallel field induction only contributes to the current density upon field reversal. We believe ignoring the induction due to the axial field is a reasonable approximation.

10. Discussion

Further development, benchmarking, and investigation into other effects are still ongoing. Upon displacement of the conductor it should be noted that the physical position of the electric currents are also displaced. The model currently maps the rotation angle onto a static pancake. Displacing the current density will have an effect although it is unknown how significant. The topic of friction was brought up in the context of edge friction as a function of axial pressure. The other important friction not considered in the calculations is the friction between each individual turn as a function of radial pressure. Coil designs have varying amounts of radial compression as a result of either preload winding tension or electromagnetic pressure. This friction should decrease the rotational strain and could be useful in high field coil designs.

11. Conclusion

We have presented a reduction in the discrepancy between measured and computed SCIF in a magnet which has significant diamagnetic twist. We have shown here that including the rotation in the calculation of the screening currrents is an important contribution towards the understanding of screening currents and the resulting SCIF and strain. Adding in the

ab-plane offset angles showed even better agreement with the measured SCIF and strain.

Data availability statement

All data that support the findings of this study are included within the article (and any supplementary files).

Acknowledgments

This work was performed at the National High Magnetic Field Laboratory, which is supported by National Science Foundation Cooperative Agreement No. DMR-1644779 and DMR-1839796, and the State of Florida.

The authors express their appreciation to the numerous people at the NHMFL and elsewhere who contributed to the design, construction, and testing of the 32 T SC magnet and the various test coils. In particular we express thanks to Bertram Green, Sanath Rama-Krishna and Arneil Reyes for their work measuring the SCIF in the 32 T SC magnet as well as Huub Weijers, Denis Markiewicz, Andy Gavrilin, Ernesto Bosque, and Edgar Berrospe-Juarez for their insight, practical discussions and inspiration.

ORCID iDs

D Kolb-Bond https://orcid.org/0000-0003-2495-0249
I R Dixon https://orcid.org/0000-0002-1163-731X
T Painter https://orcid.org/0000-0003-4106-955X
J Lu https://orcid.org/0000-0001-8521-489X
F Grilli https://orcid.org/0000-0003-0108-7235

References

[1] Brandt E H 1994 Thin superconductors in a perpendicular magnetic ac field: general formulation and strip geometry *Phys. Rev.* B **49** 9024–40
[2] Brandt E H 1996 Superconductors of finite thickness in a perpendicular magnetic field: strips and slabs *Phys. Rev.* B **54** 4246–64
[3] Gu C, Qu T and Han Z 2007 Measurement and calculation of residual magnetic field in a Bi2223/Ag magnet *IEEE Trans. Appl. Supercond.* **17** 2394–7
[4] Amemiya N and Akachi K 2008 Magnetic field generated by shielding current in high Tc superconducting coils for NMR magnets *Supercond. Sci. Technol.* **21** 095001
[5] Yanagisawa Y *et al* 2011 Magnitude of the Screening Field for YBCO Coils *IEEE Trans. Appl. Supercond.* **21** 1640–3
[6] Grilli F, Pardo E, Stenvall A, Nguyen D N, Yuan W and Gömöry F 2014 Computation of losses in HTS under the action of varying magnetic fields and currents *IEEE Trans. Appl. Supercond.* **24** 8200433
[7] Zhang M, Yuan W, Hilton D K, Canassy M D and Trociewitz U P 2014 Study of second-generation high-temperature super-conducting magnets: the self-field screening effect *Supercond. Sci. Technol.* **27** 095010
[8] Ueda H *et al* 2016 Numerical simulation on magnetic field generated by screening current in 10-T-class REBCO coil *IEEE Trans. Appl. Supercond.* **26** 4701205
[9] Pardo E 2016 Modeling of screening currents in coated conductor magnets containing up to 40,000 turns *Supercond. Sci. Technol.* **29** 085004
[10] Xia J, Bai H, Lu J, Gavrilin A V, Zhou Y and Weijers H W 2015 Electromagnetic modeling of REBCO high field coils by the H-formulation *Supercond. Sci. Technol.* **28** 125004
[11] Noguchi S, Ueda H, Hahn S, Ishiyama A and Iwasa Y-K 2019 A simple screening current-induced magnetic field estimation method for REBCO pancake coils *Supercond. Sci. Technol.* **32** 045007
[12] Berrospe-Juarez E, Zermeno V M R, Trillaud F and Grilli F 2019 Real-time simulation of large-scale HTS system: multi-scale and homogeneous models using the T-A formulation *Supercond. Sci. Technol.* **32** 065003
[13] Xia J, Bai H, Yong H, Weijers H W, Painter T A and Bird M D 2019 Stress and strain analysis of a REBCO high field coil based on the distribution of shielding current *Supercond. Sci. Technol.* **32** 095005
[14] Li Y *et al* 2019 Magnetization and screening current in an 800-MHz (18.8-T) REBCO NMR insert magnet: experimental results and numerical analysis *Supercond. Sci. Technol.* **32** 105007
[15] Kolb-Bond D J, Berrospe-Juarez E, Bird M, Dixon I R, Weijers H W, Trillaud F, Zermeno V M R and Grilli F 2020 Computing strains due to screening currents in REBCO magnets *IEEE Trans. Appl. Supercond.* **30** 4602805
[16] Li Y, Park D, Lee W, Choi Y, Tanaka H, Bascunan J and Iwasa Y 2020 Screening-current-induced strain gradient on REBCO conductor: an experimental and analytical study with small coils wound with Monofilament and striated multifilament REBCO tapes *IEEE Trans. Appl. Supercond.* **30** 4702305
[17] Takahashi S, Suetomi Y, Takao T, Yanagisawa Y, Maeda H, Takeda Y and Shimoyama J-I 2020 Hoop stress modification, stress hysteresis and degradation of a REBCO coil due to the screening current under external magnetic field cycling *IEEE Trans. Appl. Supercond.* **30** 4602607
[18] Yan Y, Xin C, Guan M, Liu H, Tan Y and Qu T 2020 Screening current effect on the stress and strain distribution in REBCO high-field magnets: experimental verification and numerical analysis *Supercond. Sci. Technol.* **33** 05LT02
[19] Berrospe-Juarez E, Trillaud F, Zermeño V M R, Grilli F, Weijers H W and Bird M D 2020 Screening currents and hysteresis losses in the REBCO insert of the 32 T all-superconducting magnet using T-A homogenous model *IEEE Trans. Appl. Supercond.* **30** 4600705
[20] Markiewicz W D *et al* 2012 Design of a superconducting 32 T magnet with REBCO high field coils *IEEE Trans. Appl. Supercond.* **22** 4300704
[21] Gurnham C W A, Große V and Hampshire D P Angular Jc measurements at 77 K in-field, on an ISD REBCO coated conductor using a straightforward mechanical scribing technique to reduce tape width *Submitted to EuCAS2019 Glasgow Conf. Proc.*
[22] Branch P *et al* 2020 Weak emergence in the angular dependence of the critical current density of the high temperature superconductor coated conductor REBCO *Supercond. Sci. Technol.* **33** 104006
[23] Lu J, Abraimov D V, Polyanskii A A, Gavrilin A V, Hilton D K, Markiewicz W D and Weijers H W 2013 Field angular dependence of hysteresis losses of coated conductor

for high field magnets *IEEE Trans. Appl. Supercond.* **23** 8200804
[24] Zhang Y *et al* 2016 Stress–strain relationship, critical strain (stress) and irreversible strain (stress) of IBAD-MOCVD-based 2G HTS wires under uniaxial tension *IEEE Trans. Appl. Supercond.* **26** 8400406
[25] Walsh R *et al* REBCO electro-mechanical properties in support of high-field magnet design *Presented ASC 2020*
[26] Brambilla R, Grilli F and Martini L 2006 Development of an edge-element model for AC loss computation of high-temperature superconductors *Supercond. Sci. Technol.* **20** 16